Using the fluctuation-dissipation theorem to measure total phase mobility during fractional flow experiments

Umar Alfazazi[1], *Marcel* Moura[2], *Ying* Da Wang[3], *Dick* Bedeaux[4], *Signe* Kjelstrup[4], *Peyman* Mostaghimi[1], and *Ryan* T. Armstrong[1*].

[1]School of Civil and Environmental Engineering, The University of New South Wales, Sydney, Australia
[2]PoreLab, the Njord Center, Department of Physics, University of Oslo, 0316 Oslo, Norway
[3]School of Minerals and Energy Resources Engineering, University of New South Wales, Sydney, Australia
[4]PoreLab, Department of Chemistry, Norwegian University of Science and Technology, NTNU, 7491 Trondheim, Norway

Abstract. This study investigates the application of the Fluctuation-Dissipation Theorem (FDT) to predict total phase mobility in two-phase flow experiments through porous media. We show that flux-fluctuations observed during steady-state multiphase flow can effectively predict total phase mobility. By analyzing these fluctuations under varying fractional flows (F_w), we construct a saturation versus total phase mobility plot and compare the results with experimental measurements obtained using Darcy's law. Additionally, the experimental system was imaged using X-ray computed microtomography, followed by image segmentation to enable direct pore-scale simulations. These simulations were used to measure relative permeability, and thus total phase mobility, offering a complementary approach to the experimental data. The agreement between simulations and experiments supports the use of FDT for measuring total phase mobility in multiphase flow systems. In general, our work highlights the potential of the FDT to convert commonly observed phase fluctuations into quantitative measures of total phase mobility, providing a novel approach to characterizing multiphase flow behavior.

1 Introduction

Multi-phase flow in porous media is an important concept encountered in many engineered and natural systems and plays an important role in various future energy processes such as subsurface CO_2, H_2 storage, and natural gas/oil recovery. Among the main descriptors of multiphase transport is relative permeability, modeled using the extended Darcy equation for two-phase flow [1]. The Darcy two-phase equation is a continuum-scale concept that relates the average fluxes of phases to the average pressure gradient. Additionally, it assumes that the fluid interfaces at the pore scale during multiphase flow in porous media are static and that the fluid configuration is in local equilibrium [2].

However, it has been observed that a static partition of fluid interfaces does not always occur, even at flow regimes dominated by capillary forces. Periodic rearrangement of the fluid interfaces has been observed for steady-state conditions [3–5], leading to fluctuations in pressure, saturation, and/or the flow rate of each phase [4, 6–9]. Since the initial observation of capillary pressure fluctuations by Yuan and Swanson [10, 11] during their experiments that involved slow-rate injection of mercury in rock samples, recent studies have provided further evidence of these fluctuations [5–7, 12, 13]. These fluctuations/oscillations have been characterized as non-thermal [14–16] and not related to experimental noise but due to complex dynamics at the pore scale where fluid clusters are forced to split and recombine. Depending on the transport phenomena and respective relaxation time the fluctuations are also called ganglion dynamics, intermittent flow or Haines jumps [4, 17–21].

Rapid fluctuations are understood to contribute to the overall fluid connectivity and thus the relative permeability of fluids [6, 19]. The most common method for determining the relative permeability is core flooding experiments by simultaneously injecting two immiscible phases at different ratios until steady state flow conditions are established for each of the defined fractional flows. The steady-state condition, sometimes also referred to as stationary flow, is defined as the flow condition in which the macroscopic properties of the system, including differential pressure and phase saturation, fluctuate around well-defined mean values. Although these fluctuations are commonly ignored in traditional core flooding studies, there is increasing evidence that they may contain information on the transport mechanisms underway, and thus on the energy dissipation.

Bedeaux and Kjelstrup [22] adopted a non-equilibrium thermodynamic approach (NET) to theoretically describe fluctuations during steady-state two-phase flow [22]. Specifically, they employed the Green-Kubo (G-K) formulation of the fluctuation dissipation theorem to characterize flux-fluctuations in a porous medium based on time- and space correlations. The FDT provides a fundamental link between fast-occurring microscopic fluctuations in a system and its macroscopic transport properties. Traditionally, FDT has been applied to homogeneous systems to determine quantities. More recently, it has been extended to complex systems, including multiphase flow in porous media [8, 14, 22].

* Corresponding author: ryan.armstrong@unsw.edu.au

Overall, the Green–Kubo formula turns the decay rate of fluctuations under stationary conditions into the linear proportionality constant (the transport coefficient) linking an applied gradient to the resulting steady flux. For multiphase flow in porous media, it has been observed that the pore-scale occupancy of fluids fluctuates under so-called steady state conditions [6, 19]. Our hypothesis herein is that the observed pore-scale fluctuations can be related to a Darcy-scale transport coefficient by using the G-K formulation. This would mean that the autocorrelation of the flux fluctuations due to capillary driven flow at the pore-scale can be related to the intrinsic resistance of a porous medium to flow.

Thus, the fluctuation dissipation theorem deals with time correlation functions of the flux-fluctuations [22]. Although the G-K formulation has been used to predict transport coefficients for various applications [23–25], it has not been used for porous media flows. Based on this, Winkler et al. [14] conducted a 2D network simulation in which fluctuations were used to investigate these correlations, which was the first study to examine the formulation of G-K for multiphase flow in porous media.

In our previous work, we compared transport coefficients (total phase mobility) determined from the G-K relations to those determined by the extended two-phase Darcy model [8]. The transport coefficient was obtained from the integral of the time-autocorrelation of the flux-fluctuations while considering the zero frequency. The comparison suggested a link between multiphase flow fluctuations and total phase mobility that substantiated the idea of using the fluctuation dissipation theorem (FDT) to study porous media flows. However, whether the established theory could provide relative permeability curves remained unanswered. How the fluctuations scaled under different fractional flows and if this scaling aligns with expected relative permeability behavior remained a pressing question.

In this paper, we conduct fractional flow experiments and quantify the resulting flux-fluctuations under stationary conditions. Fractional flow experiments are performed for a range of capillary dominated flow rates in which linear (Darcy) behavior is observed. The total phase mobility resulting from the analysis of the flux-fluctuations is then compared with both Lattice-Boltzmann relative permeability measurements and experimentally determined total phase mobility measurements.

2 Thermodynamic Description of Relative Permeability

Following the application of non-equilibrium thermodynamics (NET), transport coefficients, analogous to permeabilities in the two-phase Darcy equation, can be defined in terms of the system's entropy production. The Darcy velocity for the wetting and non-wetting phases in NET can be written as:

$$u_w = -\frac{1}{T}\left(V_w L_{ww} V_w + V_w L_{wn} V_n\right)\frac{\Delta p}{\Delta x} = -\frac{k_w K}{\eta_w}\frac{\Delta p}{\Delta x},$$
$$u_n = -\frac{1}{T}\left(V_n L_{nw} V_w + V_n L_{nn} V_n\right)\frac{\Delta p}{\Delta x} = -\frac{k_n K}{\eta_w}\frac{\Delta p}{\Delta x}, \quad (1)$$

where, u is Darcy velocity, T is temperature, V is partial volume per particle of a component, Δp is hydrostatic pressure difference, k is relative permeability of fluid, η is fluid viscosity, w, n represents wetting and non-wetting phase, K is absolute permeability. The coefficients L_{ww}, L_{nn}, L_{wn}, L_{nw}, in Equation 1 quantify the relationship between the thermodynamic forces and the resulting fluxes. L_{ww} and L_{nn} refer to the two conventional or main coefficients, while L_{wn} and L_{nw} are the cross-coupling coefficients.

In this study, we measured the total volumetric flux of the wetting and nonwetting phases J_V. Therefore, we sum the above two equations to get the average volumetric flux. As a result, we did not determine the cross-coupling coefficients and only defined the main transport coefficient, L_{VV}. In terms of the two-phase extension of Darcy's law, L_{VV} can be related to the product of the sum of the effective mobilities of both phases and the absolute permeability of the rock:

$$J_V = u_w + u_n = V_w J_w + V_n J_n = -\frac{1}{T}\left(V_w L_{ww} V_w + V_w L_{wn} V_n + V_n L_{nw} V_w + V_n L_{nn} V_n\right)\frac{\Delta p}{\Delta x} = -\frac{1}{T} L_{VV}\frac{\Delta p}{\Delta x} = -\left(\frac{k_w}{\eta_w} + \frac{k_n}{\eta_n}\right) K \frac{\Delta p}{\Delta x}. \quad (2)$$

The main transport coefficient L_{VV} (or total phase mobility) is therefore given by:

$$\frac{L_{VV}}{T} = \left(\frac{k_w}{\eta_w} + \frac{k_n}{k_n}\right) K \quad (3)$$

where k_w and k_n are the relative permeabilities, K is the absolute permeability, Δp is the pressure difference from inlet to outlet, Δx is the length of the core, and η_w and η_n are the dynamic viscosity of the wetting and nonwetting phases, respectively.

Using the G-K formulation, the transport coefficient L_{VV} can also be determined based on the fluctuation contributions $J_{V,R}$ of the fluxes over a small-time scale rather than time-averaged fluxes. The average of the fluctuation contributions to the flux is equal to zero. The G-K formulation is given by:

$$\frac{2 k_B L_{VV}}{V_L} = \int_{t'}^{\infty} dt \left\langle J_{V,R}(t) J_{V,R}(t') \right\rangle. \quad (4)$$

The right-hand side of the equation represents the autocorrelation function of flux fluctuations at stationary flow conditions, evaluated over the time difference $t - t'$. This relation implies that the magnitude of the coefficient L_{VV} depends on how long the fluctuation contributions remain correlated in time, which in turn relates to the transport coefficient of the medium.

The prefactor F is a practical ratio and is defined as:

$$F = \frac{L_{VV}/T}{\int_{t'}^{\infty} dt \langle J_{V,R}(t) J_{V,R}(t') \rangle} = \frac{V_L}{2k_B T}. \quad (5)$$

where, k_B is Boltzmann constant, and V_L is volume of the system.

It has been shown that L_{VV}, based on the fluctuation-dissipation theorem (FDT), is related to L_{VV} from the time-average fluxes by the prefactor F as shown above [8]. The integral $(\int_{t'}^{\infty} dt \langle J_{V,R}(t) J_{V,R}(t') \rangle)$ represents the integral of the time autocorrelation (ACF), which is proportional to the total phase mobility ratio of the two phases, as shown by:

$$\int ACF \propto \frac{L_{VV}}{T} = \left(\frac{k_w}{\eta_w} + \frac{k_n}{\eta_n}\right) K. \quad (6)$$

In the following, we will evaluate Equations 5 and 6 experimentally and numerically for different fractional flows.

3 Materials and Methods

First, we describe the experimental setup for measuring steady-state fractional-flow flux fluctuations. Next, we outline how the data were processed according to the theory in Section 2 and compared to the traditional two-phase Darcy law. Finally, we detail the direct pore-scale simulations used to derive the sample's relative permeability curve.

3.1 Experimental System

Two-phase co-injection experiments were conducted at room temperature, following the methodology reported by Alfazazi et al. [8]. In the following, the salient points regarding the experimental system will be provided, while further details are reserved for the Appendix. Overall, Table 1 summarizes the experiments conducted.

A sintered column of glass beads was created in a furnace by mixing 0.09 to 0.15 mm and 0.1 to 0.2 mm diameter glass beads in the same proportion, producing a cylindrical porous medium with length and diameter of 6 and 3 mm, respectively. The absolute permeability of the column to water was determined to be 8×10^{-12} m^2. The water and decane used in the experiments have densities of 997 kg/m^3 and 730 kg/m^3, respectively, and are fully immiscible. The interfacial tension was approximately 30 mN/m.

The experiments were conducted under capillary force dominated flow, where the linear Darcy law holds as confirmed in the Results section. Unlike the classic core flooding method, where experiments are conducted under constant flow rate conditions, we report experiments at constant average pressure gradient while measuring the total flow rate at the sample outlet using a mass flowmeter. This was done since the developed theory is for flux-fluctuations under a constant pressure gradient.

The BRONKHORST (BFS 1 +) mass flow meter can measure flux at an interval of 30 ms within ±2% of the measured value as specified by the manufacturer. Tests were conducted to independently confirm the calibration of the flowmeter. These tests were performed by connecting an injection pump to the flowmeter and injecting water at constant flow rates as those used in the actual experiments. The results showed agreement between the pump and flowmeter readings, with an error of less than 3.5% for all measurements. Table T1 in the Appendix summarizes the measurements conducted.

A schematic of the experimental system is shown in Figure 1. Both wetting and non-wetting phase reservoirs are supplied with constant pressure from a nitrogen gas cylinder via an ELVEFLOW (OB1 MK3+) pressure controller, which can provide accurate pressure reading with pressure stability and resolution of 0. 005% and 0. 003%, respectively, as provided by the manufacturer. Equal pressure is maintained on the surface of the fluids in both reservoirs with the aid of a T-junction connector.

The proportion of fluids flowing into the core inlet was controlled by adjusting the height difference (Δh) between the fluid levels on each reservoir. Adjusted Δh, the fluids maintained different absolute pressures at the core inlet, which subsequently resulted in a given fractional flow $F_w = Q_w/(Q_w + Q_n)$, where Q_i is the volumetric flow measured at the outlet of the sample. For the reported experiments, Δh and F_w were defined based on empirical measurements. These were achieved by generating a calibration curve of Δh versus F_w, which is provided in the Appendix.

In general, the applied pressure on the pressure controller and the Δh between the fluid columns are controlled parameters, while F_w is the output parameter determined by the set condition. Based on experiments and petrophysical measurements, we found that a 6 cm diameter of the fluid reservoir was sufficient to maintain injection at a constant F_w for 60 minutes with less than ±5% deviation from the initial saturation and F_w as specified by the calibration curve. Measurements of the systems stationarity during experiments are provided in the Appendix.

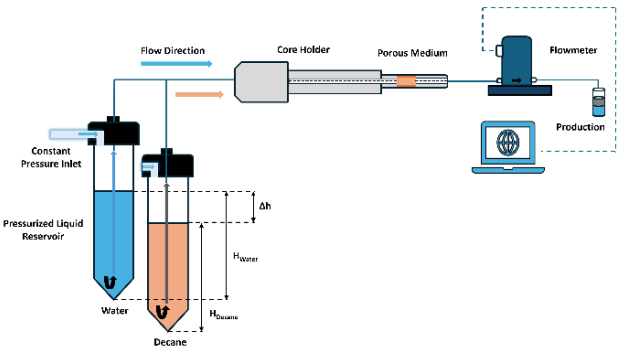

Figure 1: Schematic of the experimental apparatus used for the co-injection experiments to measure flux-fluctuations under a constant pressure gradient.

3.2 Flux Measurements

Experiments were conducted under a constant pressure gradient, with the total flux continuously measured using a mass flowmeter to enable application of the FDT. To establish a physical connection between the measured total flux and the internal dynamics in the porous medium, we compared fluctuations recorded by the mass flowmeter with the time derivative of water saturation computed from in-situ dynamic saturation acquired during the same experiment.

All experiments were conducted under a capillary force-dominated flow regime across different fractional flow conditions. The capillary number was calculated based on the average flux measured for each fractional flow condition. Specifically, q_t was calculated as the time-averaged flux over the entire duration of each time series. Using the applied injection pressures and the corresponding fractional flow values, the capillary number (Ca) was computed according to Equation 7, as described by Spurin et al. [21]:

$$Ca = \frac{q_t}{\gamma\left(\frac{1-f_w}{\eta_n} - - \frac{f_w}{\eta_w}\right)} \quad (7)$$

where q_t is Darcy average flux, γ represents the interfacial tension between the two phases, and f_w is water fractional flow determined from volumetric production data recorded during each experiment. q_t was calculated based on the average of flux of each time series measured with the mass flowmeter.

3.3 Data Analysis

A flux time series was recorded under steady-state flow conditions for different Ca and F_w. Steady-state flow (also referred to as stationary flow) is the state in which the macroscopic variables fluctuate around well-defined constant averages. The application of FDT is based on flux-fluctuations under stationary flow. Flux-fluctuations were determined by subtracting the mean flux from the flux time series data for a given stationary condition. i.e., $flux\ fluctuations = flux - mean(flux)$

Additional analyses were conducted on the time series data to confirm stationarity during the measurements. The flux data was divided into two equal segments, and the mean flux, variance, and integral ACF were calculated for each segment. Under stationary conditions, no difference should be observed between the data sets. Furthermore, volumetric production at the flow meter outlet was collected at 5-minute intervals during each experiment to calculate F_w. These measurements were done to evaluate the stationarity of the experimental system.

The time-autocorrelation function of the flux-fluctuations was determined using the autocorr function in MATLAB. For further analysis of the autocorrelation (ACF) curves, an exponential decay curve fitting was performed using the least squares method. Lastly, the integral of the ACF was determined by measuring the area under the fitted curve, which was subsequently used to determine the transport coefficient as defined in Equation 6.

The total phase mobility was also experimentally determined by using the two-phase extension of Darcy's law. Darcy behavior assumes a linear relationship between the Darcy velocity and the pressure gradient. Based on the mean total flux (J_V) measured under stationary flow, we have the following:

$$J_V = -\left(\frac{k_w}{\eta_w} + \frac{k_n}{\eta_n}\right) K \frac{\Delta p}{\Delta x}. \quad (8)$$

The total phase mobility is:

$$M_t = \left(\frac{k_w}{\eta_w} + \frac{k_n}{\eta_n}\right) K. \quad (9)$$

M_t was determined by plotting J_V versus $\frac{\Delta p}{\Delta x}$ and finding the slope using linear regression.

3.4 Relationship between Internal Core Dynamics and Measured Outlet Fluctuations

During multiphase flow, complex pore scale interactions give rise to intermittent flow patterns. In our analysis, these dynamics are interpreted as the source of flux fluctuations, which are effectively captured by a high-resolution mass flowmeter. To evaluate the internal dynamics and the measured outlet response, we compared two time-resolved quantities from the same experiment:

- Flux fluctuation time-series obtained from flowmeter by subtracting the mean from the raw flux data as expressed by: $flux\ fluctuations = flux - mean(flux)$.

- Time derivative of average S_w calculated from dynamic 2D radiograph images captured at 250-milliseconds intervals using a micro-CT. We first calculated the phase saturation from the images using the intensity-based equation:

$$S_{nw} = \frac{I_x - I_{100\%\,w}}{I_{100\,nw} - I_{100\%\,w}}, \quad (10)$$

where, S_{nw} is non-wetting phase saturation, I_x, $I_{100\,w}$, $I_{100\%\,nw}$ are image intensities of the current state, 100% wetting phase, and 100% non-wetting phase, respectively.

To evaluate wetting phase flux fluctuations from the images, we calculated the change in S_w overtime within the core volume given by:

$$F_{volume} = \frac{S_w(i+1) - S_w(i)}{\Delta t} V_{image} \phi, \quad (11)$$

where F_{volume} represents volumetric fluctuations, Δt is the time interval between two successive images, ϕ is the porosity, $V_{image} = \pi r^2 L$, is the volume of image, and $S_w(i)$, $S_w(i+1)$ represents the core average saturation at consecutive time steps.

To measure flux fluctuations, we divide the volumetric fluctuations by the cross-sectional area of the core sample:

$$J_{ff} = \frac{F_{volume}}{A_{image}}. \quad (12)$$

The resulting time-series, $J_{ff}(t)$ represents image-based flux fluctuation.

$J_{ff}(t)$ is then directly compared with the flowmeter-based flux fluctuations to evaluate if the measured flux fluctuations from the flowmeter represent the internal dynamics.

3.5 Relative Permeability Simulation

We conducted a direct simulation of relative permeability on a segmented micro-CT image of the glass bead pack used for experiments. The simulation was carried out using the code provided by the Lattice Boltzmann for Porous Media project (https://github.com/OPM). The simulation was conducted to mimic a steady-state drainage experiment using the protocols explained by [26, 27].

The micro-CT image of the sample (Figure 2) was 750 x 750 x 750 voxels with a resolution of 2.7 μm . The inlet and outlet of the domain were mirrored with a 10-slice thick transition geometry obtained by linear interpolation of the inlet and outlet geometries. The simulation was performed with periodic boundary conditions using the morphologically accelerated steady-state protocol, whereby for the case of drainage, the non-wetting phase distribution was dilated up until a 10% saturation change occurs. This was followed by normal simulation steps until the phase distributions became static under the body forces imposed (set to mimic co-injection at a capillary number of 10^{-5}, within the capillary dominated flow regime). The glass bead pack was assumed to be water wet by setting the contact angle as 40°.

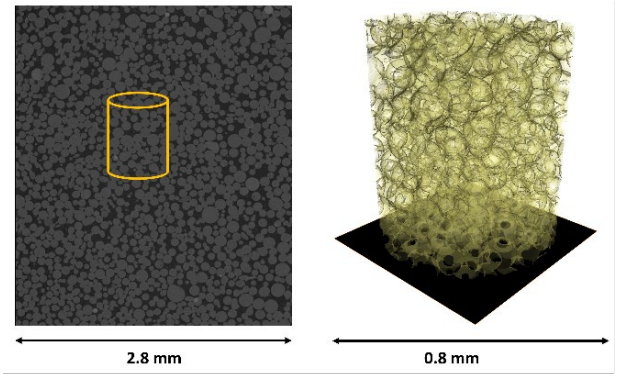

Figure 2: Segmented image of the sample used for the experiments.

The effective permeability (k_i) for each fluid is calculated as:

$$k_i = \frac{u_i \mu_i}{B_f}. \quad (13)$$

where μ_i is the fluid's dynamic viscosity, u_i is average flow velocity (normal to the domain inlet), and B_f is an external body force. The average flow velocity is defined as:

$$\langle \boldsymbol{u} \rangle_i = \frac{\boldsymbol{P}_i}{M_i}, \quad (14)$$

where $\boldsymbol{P}_i$ represents the total momentum and M_i is the total mass of fluid i. Relative permeability is therefore defined as:

$$k_{ri} = \frac{k_i}{K}. \quad (15)$$

The absolute permeability, K, is determined by a single-phase simulation on the same domain.

4 Results

First we need to explain the nomenclature that will be used throughout the remainder of this paper. Direct pore-scale simulations were used to measure the relative permeability curve of the system before any experiments. These simulations helped to guide which fractional flows to target such that experimental data could be collected at the system's minimum total phase mobility and at saturations both above and below this minimum. The terms "Target F_w" and "Target S_w" refer to the targeted values based on the simulation results. The term "Experimentally Measured F_w" was the value obtained from measuring the effluent volumes at 5-minute intervals. The term "Experimentally Estimated S_w" was obtained by using the "Experimentally Measured F_w" to determine the system saturation based on the simulated relative permeability curve that was translated into a fractional flow curve (see Appendix A2B). Therefore, we map the experimentally measured F_w on the simulated F_w vs. S_w curve to determine the corresponding S_w values. Hence, we use the term 'Estimated'.

As summarized in Table 1, the experiments were conducted at three different capillary numbers (Ca = 6.32 × 10^{-6}, 7.39 × 10^{-6}, and 9.51 × 10^{-6}) and in three different Δh settings, resulting in three corresponding F_w values. Each test was repeated in triplicate for consistency. The applied pressure drops (resulting in different Ca) were selected based on our previous work where a linear force-flux relationship was observed [8] as required by NET. Table 1 presents the average fluxes from the three runs for each set of conditions along with the standard deviation of the average fluxes, which indicates the variation observed across the triplicate experiments.

Table 1: A summary of the experiments collected with their respective average flux and standard deviation for triplicate experiments.

Target F_w	Press Drop (Psi)	Press Drop (Pa)	*Ca* x 10^{-6}	Av. Flux (m/s) x 10^{-5}	STD Divia x10^{-6}
0.8	2.0	13790	6.32	2.47	0.20
	2.5	17237	7.96	3.14	1.15
	3.0	20684	9.51	3.73	0.87
0.5	2.0	13790	6.32	2.16	0.55
	2.5	17237	7.96	2.85	0.50

	3.0	20684	9.51	3.41	1.79
0.2	2.0	13790	6.32	2.72	1.26
	2.5	17237	7.96	3.40	0.30
	3.0	20684	9.51	3.94	0.51

In addition to the fractional flow experiments, we conducted a complimentary experiment to compare the dynamic behavior captured by the flowmeter with that derived from time-resolved saturation images acquired during the same experimental run. Figure 3 overlays the image-based J_{ff} to the mass flowmeter measurements, both resampled to a 1-second interval to reduce noise. As shown in Figure 3, there is agreement in the fluctuation patterns. Particularly, in the timing, direction, and amplitude of the peaks and troughs. This indicates a correlation between the internal saturation dynamics within the pore space and the corresponding outlet flow response.

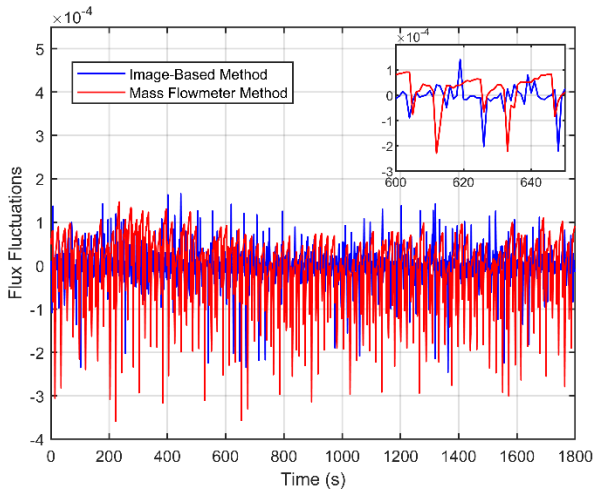

Figure 3 : Comparison of internal saturation dynamics based on CT images and fluctuations generated from flowmeter measurements.

Additionally, we computed the minimum, maximum, and standard deviation of both signals, which are summarized in Table 2. Results suggest that the outlet fluctuations are a response of internal dynamics and phase rearrangements inside the core sample. However, correlation between the internal dynamics and outlet fluctuations was likely supported by the high permeability and short sample length making it ideal for the presented work, and thus should not be expected universally for all samples and experimental setups.

While both image based and flowmeter derived methods were used to analyze the fluctuations, the flowmeter was preferred due to its greater temporal resolution. The flowmeter provides measurements at a resolution of 30-milliseconds, which aligns with the time scale of pore scale displacement events [6, 28]. In contrast, although image-based fluctuation can be acquired at time interval as short as 250-milliseconds, we observed that resampling to 1 second is required to reduce noise, which is amplified when taking the time derivative of saturation.

Table 2: Statical comparison between internal saturation change and fluctuations generated from flowmeter at the outlet.

	Image Based Fluctuations	**Flowmeter Based Fluctuations**
Min value	-2.46 x 10^{-4}	-3.59 x 10^{-4}
Max value	1.66 x 10^{-4}	1.47 x 10^{-4}
STD	3.80 x 10^{-5}	7.40 x 10^{-5}

Figure 4 shows the linear relationship between the average flux at the respective pressure drops for the experiments carried out for F_w = 0.2, 0.5, and 0.8. The regression fit was forced to pass through the origin and the R^2 for each F_w was greater than 0.99. Therefore, the average fluxes are consistent with Darcy flow behavior. Based on these results, we can determine M_t for each fractional flow. The M_t calculated for the values of F_w of 0.2, 0.5, and 0.8 were 1.02 x 10^{-11}, 1.09 x 10^{-11}, and 1.07 x 10^{-11} $m^2/Pa \cdot s$, respectively.

To evaluate stationarity during our experiments, we divided the time series data for each experiment into two segments. Under stationary conditions, each segment should yield the same average flux. As shown in Table T2 in the Appendix section, the average flux, variance, and integral ACF were calculated for each pair of segments for the experiments. The percentage change in variance between the segments and the entire time series for each experiment ranges from -10% to $+6\%$. This variation is attributed to experimental limitations, as the experimentally measured F_w slightly changed during the experiments. Additional analysis is presented in Table 3, which summarizes the uncertainty in the fractional flow and the corresponding saturation for each experiment, which shows that the uncertainties associated with these measurements are comparable to the uncertainty in our stationarity analysis.

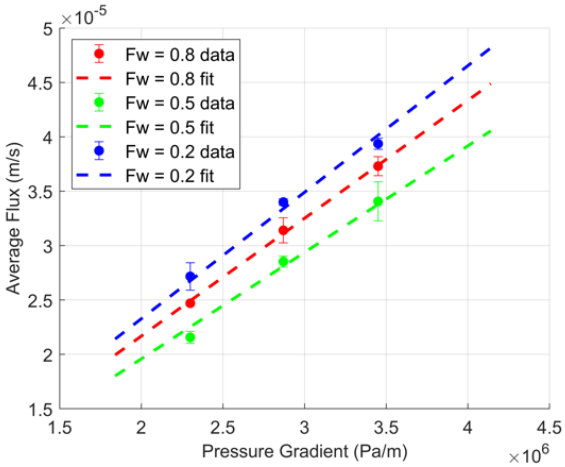

Figure 4: Experimentally measured average fluxes as a function of pressure gradient, measured at different fractional flows.

In addition to our stationarity analysis, Figures 5A-F demonstrate typical flux data collected from the mass flow meter. It is seen that the behavior of the fluctuations remains consistent with respect to time for all the experiments, aligned with our previous assessment of stationarity. In addition, fluctuations appear to occur at all fractional flows, demonstrating the influence of capillarity under fractional flow conditions. Fluctuations were also measured at F_w = 1.0 (results provided in Appendix Table T1) demonstrating that the fraction flow fluctuations exceed that for single phase flow.

Next, we computed the autocorrelation of the flux-fluctuations. Several oscillations are evident from the ACF, which decay with time. The oscillations are attributed to different transport mechanisms (or modes), such as energy accumulation and release, over periodic time scales. The impact of these oscillations on transport behavior is beyond the scope of this work but should be considered in future work. Based on the figures, it can be observed that at F_w = 0.5, there are more oscillations, thus, more intermittency compared to the experiments reported at F_w = 0.2 and 0.8. Similar results have been reported elsewhere [4, 7, 13, 21]. Rucker et al. [7] presented results from pressure fluctuations during water and oil co-injection experiments at different fractional flows. They found that the fluctuations caused by the intermittent flow behavior are more apparent at intermediate fractional flow. However, from our observations, these oscillations result in a negative autocorrelation, presumably reducing the total phase mobility. This observation is aligned with typical relative permeability curves where M_t is at a minimum for intermediate saturation.

Table 3: Summary of average integral auto correlation function at different pressure drops and fractional flow.

Pressure	Δh	Target	Experimentally	Target	Experimentally	$\int ACF$	% Uncertainty
(Pa)	(m) x10^{-2}	F_w	Measured F_w	S_w (%)	Measured S_w (%)	(m^2/s) x10^{-11}	
13790	0.65	0.2	0.2 ± 0.01	44	44 ± 1	2.78	7.4
	2.30	0.5	0.5 ± 0.03	57	57 ± 2	2.30	0.9
	4.70	0.8	0.8 ± 0.05	70	70 ± 2	3.86	2.4
17237	0.65	0.2	0.2 ± 0.01	44	44 ± 1	2.80	14.1
	2.30	0.5	0.5 ± 0.05	57	57 ± 2	2.58	0.4
	4.70	0.8	0.8 ± 0.02	70	70 ± 1	3.51	7.4
20684	0.65	0.2	0.2 ± 0.03	44	44 ± 2	2.89	6.8
	2.30	0.5	0.5 ± 0.03	57	57 ± 2	2.40	7.8
	4.70	0.8	0.8 ± 0.04	70	70 ± 2	3.32	11.0

To determine the transport coefficient from the Fluctuation-Dissipation Theorem (FDT), we calculated the area under the autocorrelation function (ACF) curve. Due to the periodic oscillations in the ACF, we calculate the integral by adopting a zero-frequency model and fitting the curve with an exponential decay function using the least-squares method. This was performed to capture the zero-frequency decay rate of the fluctuations while the higher frequency oscillations were assumed to have a negligible contribution to the transport coefficient.

Table 3 summarizes the average of the integral of the ACF for the triplicate experiments at their respective F_w and S_w. Figure 6 also displays these values with respect to S_w. To ensure consistency in the zero-frequency model adopted in Figure 5 B, D and F, the ACF fitting was performed at different lag time intervals (i.e. lags between 0-500, 0-1000, 0-2000, and 0-3000 s) as shown in the Appendix A3, which showed consistency in the results. Based on these results, we present the findings of our work using a time interval of 0-1000 s.

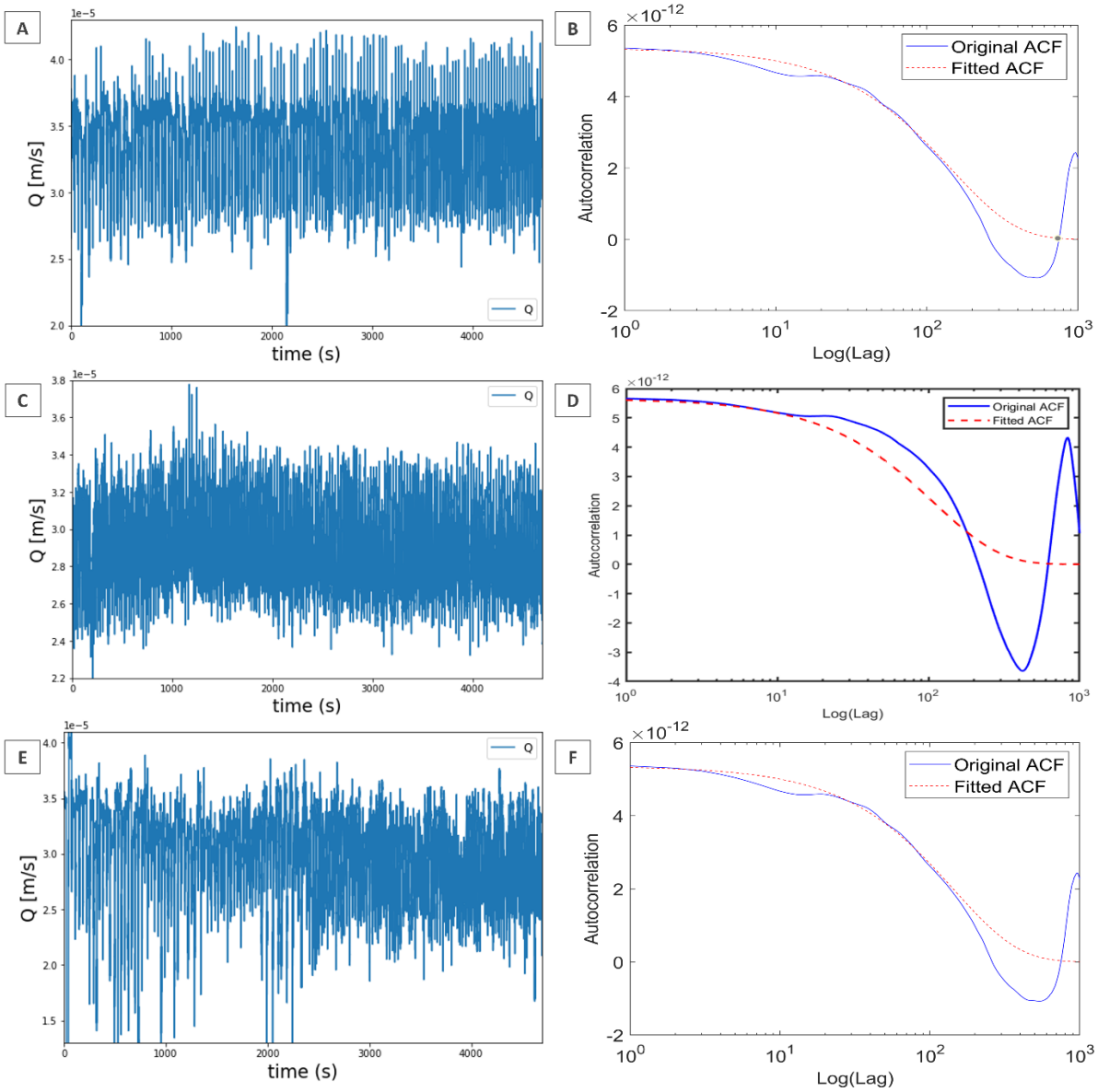

Figure 5: Typical flow time series data for experiments conducted at 17237 Pa at different fractional flow. **A-B.** Time series data and ACF for experiment at F_w = 0.2. **C-D.** Time series data and ACF for experiment at F_w = 0.5. **E-F**. Time series data and ACF for experiment at F_w = 0.8.

The relationship provided in Equation 6 can be investigated first by plotting both $\int ACF$ and M_t against S_w. If $\int ACF$ indeed represents M_t through a proportionality, then both measures should scale with phase saturation in the same way. As observed in Figure 6, both terms follow similar behaviors that correspond to saturation. Overall, the present results show that the FDT-derived coefficients remain consistent with Darcy's equation at different F_w values. However, the proportionality constant, F, remains elusive based on the analysis presented in Figure 6.

To estimate F, we take an empirical approach. Figure 7 shows the relationship between M_t and the $\int ACF$ for the three capillary numbers studied at different water saturations. For the tested range of Ca values, the slope, i.e. F, remains nearly the same, based on triplicate measurements as presented in Table 3. A linear fit to this data also provides interesting insight into the application of Green-Kubo to our experimental system. The fit does not appear to go through the origin but instead is offset by a y-intercept of 2.2 x 10^{-12} $m^2/\text{Pa} \cdot s$. In principle, the integration in Equation 4 is from the molecular scale, i.e., femtoseconds and higher. However, experimentally, fluctuations down to 30 milliseconds was the limit of our mass flow meter. We therefore propose the following relationship.

$$c + F_e \int_{exp}^{\infty} ACF = \left(\frac{k_w}{\eta_w} + \frac{k_n}{\eta_n}\right) K, \qquad (16)$$

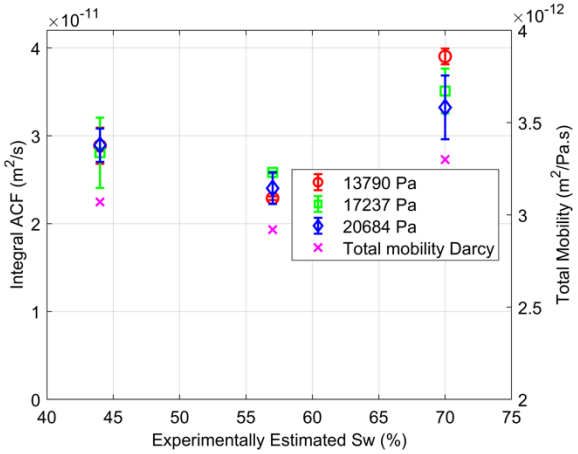

Figure 6 : Average integral of the auto-correlation function based on flux-fluctuations across triplicate experiments and total mobility based on the two-phase extension of Darcy's law versus water saturation.

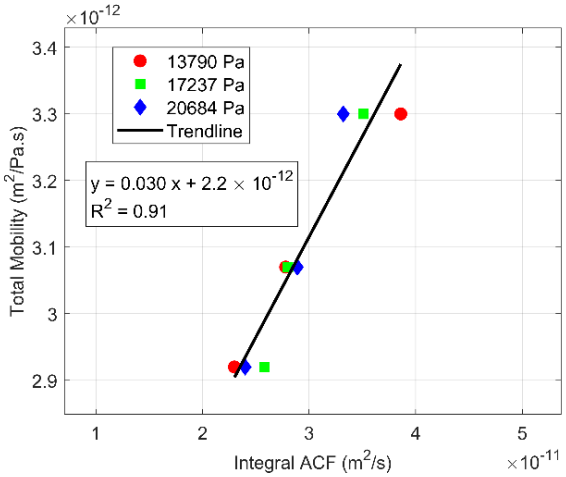

Figure 7: Average total Mobility versus average of the integral of the ACF for all experiments.

Where c is a constant ($c \propto \int_{femto}^{exp} ACF$) and F_e is the experimentally determined pre-factor; these parameters are required because the mass flow meter cannot measure fluctuations less than 30 milliseconds.

For the experimental results, we have $c = 2.2 \times 10^{-12}\ m^2/\text{Pa} \cdot s$ and $F_e = 0.03\ \text{Pa}^{-1}$. Between the femtosecond to millisecond time scales, the associated fluctuations would be molecular in origin and mostly associated with the viscosity of the fluids and the influence of the porous domain. However, for millisecond and upward time scales, associated fluctuations would be capillary in origin and associated with pore-scale displacements, and thus fractional flow condition [12, 28, 29]. Based on this analysis, a significant fraction of total phase mobility comes from the phase viscosity and influence of the pore structure, while the remaining fraction is capillary in origin. This is well aligned with the Darcy concept where K, η_w and η_n would be captured by the faster time scales and k_i would be captured by the slower time scale, possibly milliseconds and higher, and thus explains how the fluids inhibit the flow of each other under the prevailing capillary conditions.

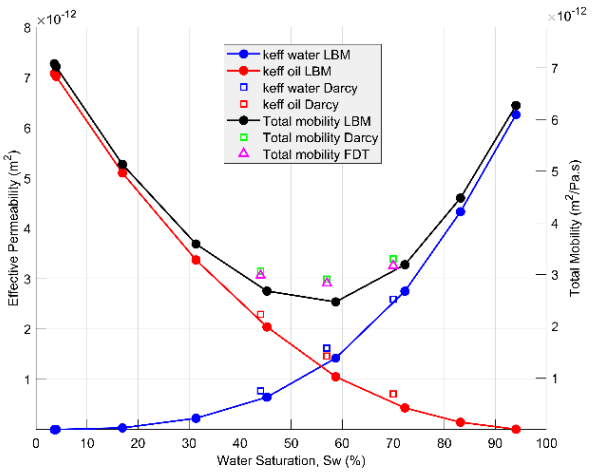

Figure 8: A comparison of effective permeability and total phase mobility determined from LBM, FDT, and Darcy.

Based on the relationship established in Figure 7, we now present effective permeability and total mobility curves based on the G-K approach. Effective permeability is defined as the product of relative permeability and absolute permeability; see Equation 15. Figure 8 presents the relationship between effective permeability and total mobility as functions of water saturation, comparing the results of the LBM simulation, Darcy's law, and FDT. Overall, there is consistency of the total mobility measurements using these three independent measurements.

5 Conclusions

We successfully demonstrate the potential of the FDT to predict transport coefficients and total phase mobility in multiphase flow through porous media. Using flux-fluctuations measured during steady-state flow experiments, we show that FDT-derived phase mobilities align closely with experimentally determined values using the traditional Darcy formulation and lattice Boltzmann simulations. This substantiates the applicability of FDT in characterizing dynamic transport behaviors, particularly in the context of capillary-dominated flow regimes.

The findings highlight the connection between the autocorrelation of pore-scale flux fluctuations and the total resistivity of a medium to flow. This provides a new perspective on understanding the complex pore-scale dynamics within porous media [22].

Further research can build on these results by refining the relationship between flux-fluctuations and relative permeability under varying flow conditions and pore-scale structures. Future work should also focus on how the cross-correlation of phase flux-fluctuations can be used to measure the Onsager cross-coupling coefficients, which provides an exciting way of studying multiphase flow systems that is not provided by the traditional Darcy formulation.

6 Appendix

The fluids were introduced into the porous medium through a 1/16" PTFE plastic tube that starts at the bottom of each reservoir and travels upward to the inlet of the core holder. By default, the fluid reservoirs were positioned at a height below the core holder (as shown in Figure 1), at which the fluids enter the porous medium. The relative height (Δh) of the fluid columns in the reservoir can be adjusted to control the fractional flow F_w through the core. The fractional flow was measured during the experiments by taking periodic volumetric measurements at the mass flow meter outlet at 5-minute intervals.

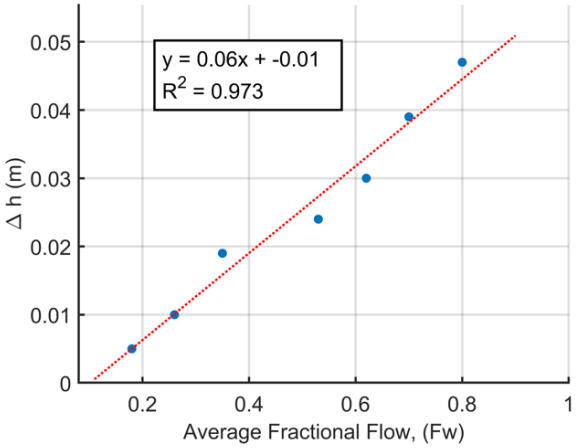

Figure A1: Calibration curve used for obtaining Δh for a desired F_w.

A calibration curve was generated by plotting the experimentally obtained values of F_w versus Δh, see Figure A1. Δh in the equation was defined as $h_{non-wetting} - h_{wetting}$, where $h_{non-wetting}$ and $h_{wetting}$ were the heights measured from the fluid surface (datum) to the core inlet.

6.1 Baseline Measurements

Simulations of relative permeability were run to design the experiments at well-controlled total phase mobilities, M_t. The following steps were followed for the experimental design:

- Pore-scale simulations of the relative permeability as a function of water saturation were carried out on the segmented micro-CT image of the sample.
- Based on the simulated relative permeability curve shown in Figure A2-A, the fractional flow curve versus water saturation Figure A2-B was calculated by:

$$F_w = \frac{1}{1+\left(\frac{k_{rn}/\eta_n}{k_{rw}/\eta_w}\right)}. \qquad (17)$$

Here, k_{rn} *and* k_{rw} represent the relative permeabilities of the nonwetting and wetting phases, while η_n and η_w are the dynamic viscosities of the nonwetting and wetting phases.

- From the fractional flow curve, the values F_w of 0.2, 0.5, and 0.8 were set as targets and their corresponding water saturation was traced from the curve. The corresponding S_w values were 44%, 57%, and 70%, respectively.
- The experimentally measured F_w values were then used to find the corresponding water saturation during fractional flow experiments. The average of the lower and upper values of S_w for each experiment was then used to calculate the deviation from the target S_w, as summarized in Table 3 of the Results section, noted as 'Experimentally Estimated S_w'.

Figure A2 shows the simulated k_r curves used for the calculations mentioned above. Water saturation was not measured directly. We assumed that at steady-state flow, the fractional-flow data represents a stable distribution of the phases. Therefore, we traced the experimentally measured F_w on the simulated fractional flow curve and read the corresponding S_w. We therefore report this value as an" Experimentally Estimated S_w".

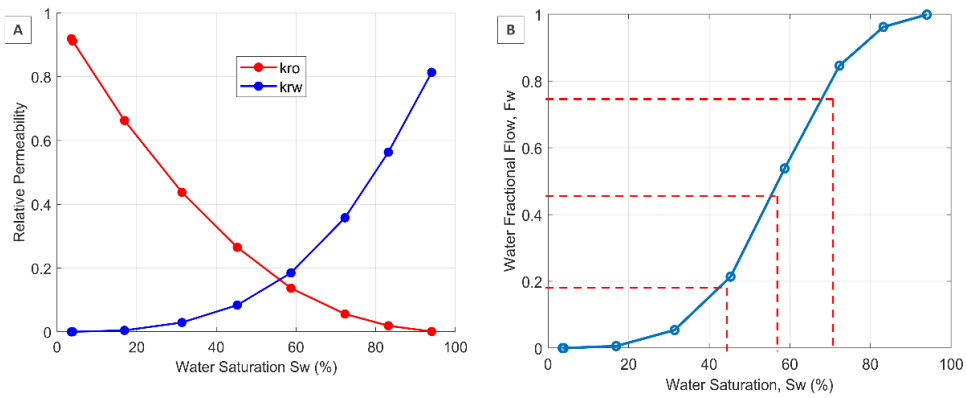

Figure A2: Pore-scale simulation on a micro-CT image of the sample used. A. Relative permeability B. Fractional flow.

6.2 Flowmeter Calibration and Validation

A quality check was performed to verify the calibration of the flowmeter. This was accomplished by connecting a syringe pump to the flowmeter and injecting water at different constant flow rates, while simultaneously recording the flowmeter output and measuring volumetric production. Table T1 presents the results of the calibration tests, comparing the injection pump rates, average flowmeter readings, and effluent volumes. The selected flow rates correspond to those used in the reported experiments and were chosen based on the targeted capillary numbers. Each flow rate was measured in triplicate to ensure repeatability.

Table T1: Flowmeter calibration test results showing comparison between pump injection rates, flowmeter readings, and effluent production, with associated percentage errors

Exp.	Pump Injection Rate (ml/min)	Average Flowmeter Rate (ml/min)	Volume production (ml/min)	Error (%)
1	0.2	0.194	0.2	3.00
2	0.3	0.290	0.3	3.30
3	0.4	0.391	0.4	2.25
4	0.5	0.491	0.5	1.80

6.3 Assessment of Stationarity

A stationarity analysis was conducted by dividing the flux time series into two equal segments and calculating their respective mean, variance, and integral ACF. If the time series data were non-stationary, we would expect the mean and the variance to vary between the two segments. However, the calculated parameters were nearly stable across all experiments. Table T2 summarizes the analyses conducted to show consistency between the different segments of the flow time series data recorded.

Table T2: Summary of data segments with the calculated average fluxes, variances, and integral ACF for each segment of the data calculated at different fractional flows and at pressure drop of 17237Pa.

F_w	Data Segment	Flux (m/s) x10^{-5}	Variance (Flux) x10^{-12}	% Change Variance	$\int ACF$ (m^2/s) x10^{-11}
0.2	All data	3.43	5.45	-	2.59
	Segment 1	3.45	4.99	-8.4	2.34
	Segment 2	3.42	5.71	4.8	2.88
0.5	All data	2.90	5.68	-	2.59
	Segment 1	2.94	5.11	10.0	2.60
	Segment 2	2.86	5.91	4.1	2.60
0.8	All data	3.15	6.36	-	3.25
	Segment 1	3.18	6.74	6.0	3.52
	Segment 2	3.13	6.29	-1.1	3.21

The fitting of the ACF curve was performed for different time intervals (0-500, 0-1000, 0-2000, and 0-3000 s) to verify consistency of the resulting ACF integral computation. Figure A3 shows the ACF integral as a function of lag for F_w of 0.2, 0.5, and 0.8 at an applied pressure of 17237 Pa. The analysis was consistent across all time intervals with only a minor difference for the first time interval between 0-500 s. The change in the integral of the ACF for the other time interval was negligible, ~1%.

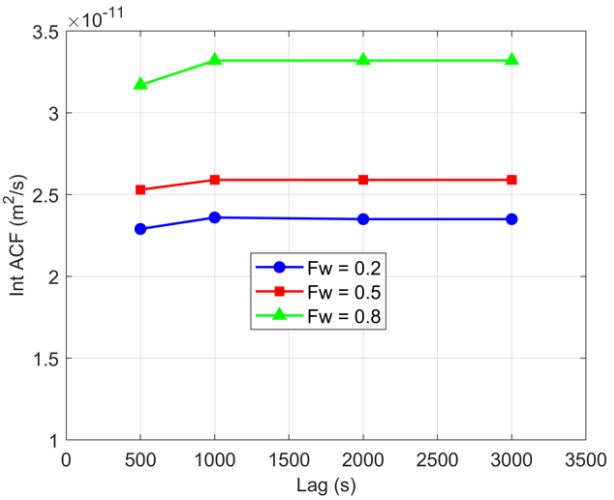

Figure A3: Integral ACF vs Lag for different F_w, at pressure drop of 17237 Pa.

M. M. acknowledges the support of the Researcher Project for Young Talents Funding Scheme of the Research Council of Norway, Project No. 324555. R. T. A. acknowledges his Australian Research Council Future Fellowship (FT210100165). D.B and S.K are grateful to the Center of Excellence Funding Scheme of the Research Council of Norway, project no 262644 Porelab.

References

1. Wyckoff, R.D., Botset, H.G.: The flow of gas-liquid mixtures through unconsolidated sands. Physics (College Park Md). 7, 325–345 (1936)
2. Blunt, M.J.: Multiphase flow in permeable media: A pore-scale perspective. Cambridge university press (2017)
3. Reynolds, C.A., Menke, H., Andrew, M., Blunt, M.J., Krevor, S.: Dynamic fluid connectivity during steady-state multiphase flow in a sandstone. Proceedings of the National Academy of Sciences. 114, 8187–8192 (2017)
4. Spurin, C., Bultreys, T., Bijeljic, B., Blunt, M.J., Krevor, S.: Intermittent fluid connectivity during two-phase flow in a heterogeneous carbonate rock. Phys Rev E. 100, 43103 (2019)
5. Gao, Y., Raeini, A.Q., Blunt, M., Bijeljic, B.: Dynamic fluid configurations in steady-state two-phase flow in Bentheimer sandstone. Phys. Rev.E. 103, 13110 (2021)

6. Berg, S., Ott, H., Klapp, S.A., Schwing, A., Neiteler, R., Brussee, N., Makurat A.and Leu, L., Enzmann, F., Schwarz, J.-O., Kersten, M., Irvine, S., Stampanoni, M.: Real-time 3D imaging of Haines jumps in porous media flow. Proceedings of the National Academy of Sciences of the U.S. 110, 3755–3759 (2013)
7. Rücker, M., Georgiadis, A., Armstrong, R.T., Ott, H., Brussee, N., van der Linde, H., Simon, L., Enzmann, F., Kersten, M.: The Origin of Non-Thermal Fluctuations in Multiphase Flow in Porous Media. Frontiers in Water. 3, 671399 (2021)
8. Alfazazi, U., Bedeaux, D., Kjelstrup, S., Moura, M., Ebadi, M., Mostaghimi, P., and James E. McClure, Armstrong, R.: Interpreting pore-scale fluctuations: Predicting transport coefficients in multiphase flow through porous media using the Green–Kubo formulation. An experimental investigation. Phys. Fluids. 36, 36616 (2024)
9. Moura, M., Bedeaux, D., Armstrong, R.T., Kjelstrup, S.: Fluctuation-dissipation theorems and the measurement of the Onsager coefficients for two-phase flow in porous media. arXiv preprint arXiv:2410.03661. (2024)
10. Yuan, H.H.: Pore-scale heterogeneity from mercury porosimetry data. SPE Formation Evaluation. 6, 233–240 (1991)
11. Yuan, H.H., Swanson, B.F.: Resolving pore-space characteristics by rate-controlled porosimetry. SPE Formation Evaluation. 4, 17–24 (1989)
12. DiCarlo, D.A., Cidoncha, J.I.G., Hickey, C.: Acoustic measurements of pore-scale displacements. Geophys Res Lett. 30, (2003)
13. Spurin, C., Bultreys, T., Rücker, M., Garfi, G., Schlepütz, C.M., Novak, V., Berg, S., Blunt, M.J., Krevor, S.: Intermittent fluid connectivity during two-phase flow in a heterogeneous carbonate rock. Water Resour Res. 56, e2020WR028287 (2020)
14. Winkler, M., Gjennestad, M.A., Bedeaux, D., Kjelstrup, S., Cabriolu, R., Hansen, A.: Onsager-Symmetry Obeyed in Athermal Mesoscopic Systems: Two-Phase Flow in Porous Media. Front Phys. 8, 60 (2006)
15. McClure, J.E., Fan, M., Berg, S., Armstrong, R.T., Berg, C.F., Li, Z., Ramstad, T.: Relative Permeability as a stationary process: energy fluctuations in immiscible displacement. Physics of Fluids. 34, 92011 (2022)
16. Bedeaux, D., Kjelstrup, S., Schnell, S.K.: Nanothermodynamics: Theory and Applications. World Scientific (2023)
17. Rücker, M., Armstrong, R.T., Georgiadis, A., Ott, H., Simon, L., Enzmann, F., Kersten, M., de Wit, S.: The Fate of Oil Clusters During Fractional Flow: Trajectories in the Saturation-Capillary Number Space. In: International Symposium of the Society of Core Analysts held in St. John's Newfoundland and Labrador, Canada, 16-21 August (2015)
18. Armstrong, R.T., Berg, S.: Interfacial velocities and capillary pressure gradients during Haines jumps. Phys Rev E. 43010 (2013)
19. Armstrong, R.T., McClure, J.E., Berrill, M.A., Rücker, M., Schlüter, S., Berg, S.: Beyond Darcy's law: The role of phase topology and ganglion dynamics for two-fluid flow. Phys Rev E. 94, 43113 (2016)
20. Haines, W.B.: Studies in the physical properties of soils. V. The hysteresis effect in capillary properties, and the modes of water distribution associated therewith. J Agric Sci. 20, 97–116 (1930)
21. Spurin, C., Bultreys, T., Rücker, M., Garfi, G., Schlepütz, C.M., Novak, V., Berg, S., Blunt, J.M., Krevor, S.: The development of intermittent multiphase fluid flow pathways through a porous rock. Adv Water Resour. 150, 103868 (2021)
22. Bedeaux, D., Kjelstrup, S.: Fluctuation-dissipation theorems for multiphase flow in porous media. Entropy. 24, 46 (2021)
23. Hauge, E.H., Martin-Löf, A.: Fluctuating hydrodynamics and Brownian motion. J Stat Phys. 7, 259–281 (1973)
24. Ben-Isaac, E., Park, Y., Popescu, G., Brown, F.L.H., Gov, N.S., Shokef, Y.: Effective temperature of red-blood-cell membrane fluctuations. Phys Rev Lett. 106, 238103 (2011)
25. Karki, B.B., Stixrude, L.P.: Viscosity of MgSiO3 liquid at Earth's mantle conditions: Implications for an early magma ocean. Science (1979). 328, 740–742 (2010)
26. McClure, J.E., Li, Z., Berrill, M., Ramstad, T.: The LBPM software package for simulating multiphase flow on digital images of porous rocks. Comput Geosci. 25, 871–895 (2021)
27. Wang, Y.D., Chung, T., Armstrong, R.T., McClure, J., Ramstad, T., Mostaghimi, P.: Accelerated computation of relative permeability by coupled morphological and direct multiphase flow simulation. J Comput Phys. 401, 108966 (2020)
28. Mohanty, K.K., Davis, H.T., Scriven, L.E.: Physics of oil entrapment in water-wet rock. SPE Reservoir Engineering. 2, 113–128 (1987)
29. Moebius, F., Or, D.: Interfacial jumps and pressure bursts during fluid displacement in interacting irregular capillaries. J Colloid Interface Sci. 377, 406–415 (2012)